Int. J. Electrochem. Sci., 12 (**2017**) 7786 – 7794, doi: 10.20964/2017.08.22

International Journal of
ELECTROCHEMICAL
SCIENCE
www.electrochemsci.org

One-Step Electrodeposition of CuZnSn Metal Alloy Precursor Film Followed by the Synthesis of Cu_2ZnSnS_4 and $Cu_2ZnSnSe_4$ Light Absorber Films and Heterojunction Devices

A.E. Rakhshani[1,*]*, A. Bumajdad*[2]*, F. Al-Sagheer*[2]*, S. Thomas*[1]*, P.H. Tharayil*[1]

[1] Department of Physics, Faculty of Science, Kuwait University, Safat 13060, Kuwait
[2] Department of Chemistry, Faculty of Science, Kuwait University, Safat 13060, Kuwait
[*]E-mail : ali.rakhshani@ku.edu.kw; alirakhshani@yahoo.com

Received: 16 April 2017 / *Accepted:* 26 May 2017 / *Published:* 12 July 2017

CuZnSn metallic alloy precursor films were electrodeposited on Mo substrate from a Zn-rich bath solution yielding low deposition rates. The precursor films were converted to photovoltaic absorber films of Cu_2ZnSnS_4 and $Cu_2ZnSnSe_4$ by sulfurization and selenization processes. X-ray diffraction, Raman spectroscopy and photocurrent spectroscopy techniques were utilized for the identification of films. The surface morphology, uniformity and compactness of the films were examined by scanning electron microscopy. The precursor and absorber films had a uniform and compact structure. The precursor films were composed from the Cu_3Sn, Cu_6Sn_5 and Cu_5Zn_8 phases and their grain size varied tightly with the cathode potential. The conversion of precursor films to Cu_2ZnSnS_4 and $Cu_2ZnSnSe_4$ were verified from the results of their X-ray diffraction, Raman shifts, and optical transition energies. To assess the device quality of the absorber films, CdS/Cu_2ZnSnS_4 and $CdS/Cu_2ZnSnSe_4$ heterojunction diodes were fabricated and their device parameters were determined. The diodes showed relatively good ideality factor of 1.3-1.9, current rectification factor of ~120, and reverse biased saturation current of ~30-60 $\mu A/cm^2$. Photocurrent spectroscopy was utilized to evaluate the band gap energy and other optical transition energies of the absorber films from the short-circuit photocurrent of the diodes.

Keywords: CZTS; CZTSe; electrodeposition; photocurrent; Raman

1. INTRODUCTION

Copper zinc tin sulfide, Cu_2ZnSnS_4 (CZTS), and copper zinc tin selenide, $Cu_2ZnSnSe_4$ (CZTSe), are intrinsically p-type semiconductors with a free hole concentration in the range of 10^{16} - 10^{20} cm^{-3} and high optical absorption coefficient ($>10^4$ cm^{-1}) which makes these materials attractive for

use as the absorber layer in thin film solar cells [1-3]. One of their distinguished characteristics, particularly in the case of CZTS, is that they consist from the abundant and non toxic elements as compared to other light absorber materials that are being used for the same purpose. The direct band gap energy of the alloy compound $CZTS_xSe_{1-x}$ can be tuned from ~0.9 eV (x = 0) to ~1.6 eV (x = 1) which renders the material even more attractive for the fabrication of tandem solar cells. The conversion efficiency of thin solar cells based on solution-grown $CZTS_xSe_{1-x}$ films has reached to 12.6% [4]. Although the CZTS and CZTSe films can be prepared by a variety of techniques, the solution based methods such as spray pyrolysis [5], electrodeposition [6], and spin coating [7] are attractive because they are simple, scalable, low-cost and non-vacuum processes. Electrodeposition of these quaternary films can be achieved by sulfurization or selenization of the electrodeposited precursor metallic alloy film of CuZnS (CZT). The precursor film can be prepared by sequential electrodeposition of Cu, Zn, and Sn stacked elemental layers or by co-electrodeposition of CZT film from a single bath solution. The sequential layer deposition requires the use of different bath solutions that involves more preparation steps and the material wastage as compared with the co-eletrodeposition route. Co-electrodeposition of CZT has been reported at a cathode potential in the range of -1.1 to -1.4 V (vs. Ag/AgCl) from a variety of solutions in which the ionic concentrations of Cu, Zn, and Sn varied in the range of 10-40 mM [8-14]. The CZTS-based photovoltaic cells prepared in this way have attained an efficiency of 6.3% [14] and the cells based on CZTSe an efficiency of 8% [10]. In an attempt to enhance the compactness of the precursor films, electrodeposition of CZT was performed at low deposition rates by using a bath solution containig much lower Cu and Sn ion concentrations as compared to the reported values [8-14]. The solution was chosen to be highly rich in Zn to enhance the deposition rate of Zn through its diffusion component at a cathode potential of -1.10 V to -1.20 V, that is in the vicinity of the Zn reduction potential. This was to suppress the rate of hydrogen evolution at the cathode that yields porous films. Here, we report on the properties of the precursor CZT and the synthesized of CZTS and CZTSe films and their device application.

2. EXPERIMENTAL PROCEDURE

For the preparation of the bath solution reagent grade $CuSO_4.5H_2O$, $ZnSO_4.7H_2O$, $SnCl_2$, and $Na_3C_6H_5O_7$ (tri-sodium citrate) complexing agent were dissolved in 18-MΩ doubly distilled water with the molecular concentrations of 6 mM, 200 mM, 3 mM, and 200 mM, respectively. Co-electrodeposition of CZT films was performed in a conventional three electrode assembly consisting from a Ag/AgCl reference electrode, and platinum counter electrode. The working electrode was Mo foil pre-cleaned and treated in ammonia solution. Co-electrodeposition was performed at a working potential of -1.10 V to -1.20 V for 20 minutes using a potentiostat unit (Autolab PGSTAT100). The CZT precursor film underwent a soft annealing procedure at 310 °C in the atmospheric pressure of argon for 80 minutes before the sulfurization or selenization process. The precursor CZT films were converted to CZTS in a closed graphite box containing 0.25 g of sulphur powder. The box was placed in a tube furnace and the temperature was raised slowly from room temperature to 580 °C under the argon flow (purity, 99.999%). After 120 min of sulfurization at 580 °C the furnace was switched off to cool down naturally to room temperature under the argon flow. A similar procedure was adopted for

the selenization of precursor films. The closed graphite box contained the sample and 0.5 g of Se. The selenization temperature and its duration were 540 °C and 15 min, respectively. Scanning electron microscopy, SEM (Jeol JSM 7001F), X-ray diffraction, XRD (Siemens D500, CuK_{α}: 0.154056 nm), Raman spectroscopy (Renishaw inVia, excitation wavelength 514 nm) and photocurrent spectroscopy techniques were used for the characterization of samples.

Heterojunction diodes were fabricated by chemical bath deposition of CdS (50-100 nm) on CZTS and CZTSe films. This was followed by a brief heat treatment in air (100 °C, 10 min) and in prior to the deposition of Al electrodes (30 nm, 1-2 mm diameter) which made ohmic contact to CdS. The chemical bath used for the deposition of CdS was an alkaline solution made of $CdCl_2$ (1.9 mM), $SC(NH_2)_2$ (3.8 mM), NH_4Cl (15.7 mM) and NH_4OH (0.85 mM). The current-voltage (IV) characteristics of the diodes were measured by a source/measure unit (Keithley 236) and their short-circuit photocurrent, normalized to the incident photon flux, was measured at different incident wavelengths using a setup consisting of a monochromator (Sciencetech 9050), lock-in amplifier (Stanford Research SR 530), current amplifier (Keithley 428), mechanical chopper and visible light source.

3. RESULTS AND DISCUSSION

3.1. CZT precursor films

Precursor CZT films with a thickness of 500- 1100 nm were electrodeposited at the cathode potential of -1.10 V, -1.15 V and -1.20 V. Fig. 1 shows the SEM plan views and the XRD plots of these films after the soft annealing process. As evident from Fig. 1(a), the compact and non-porous CZT films were composed from grains with a size that varied with the deposition potential as 140 nm (-1.10 V), 280 nm (-1.15 V) and 670 nm (-1.20 V). The increase of the grain size may partly be due to the increase of the film thickness from ~470 nm (-1.1 V) to ~1100 nm (-1.20 V) during the same deposition time of 20 min. Fig. 1(b), illustrating the XRD patterns of the CZT films, indicates that the films are composed from the Cu-Sn and Cu-Zn alloys with chemical compositions of Cu_6Sn_5 (JCPDS 65-2303), Cu_3Sn (JCPDS 65-4653), and Cu_5Zn_8 (JCPDS 41-1435) in addition to metallic Sn (JCPDS 65-2631). The XRD line at $2\theta = 47.8°$ (*) may indicate the presence of the CuCl trace impurity phase. The average size of crystallites that form the grains, L, was estimated from the full width at half maximum, β, of the diffraction line at $2\theta = 43.1°$ (assigned to Cu_6Sn_5 and Cu_5Zn_8) and using the Scherrer equation $L = 0.94\ \lambda/(\beta\ \cos\theta)$, where λ (= 0.15406 nm) is the wavelength of the incident X-ray [15]. The L value obtained for the CZT films was 24-28 nm and independent from the deposition potential. The precursor films with the large grain structure deposited at -1.20 V were used for the sulfurization and selenization processes.

3.2. CZTS films

Fig. 2(a) shows the XRD spectrum and SEM plan view (inset) of a sulfurized precursor film. Sulfurization lead to the growth and coalescence of grains. The CZTS films were uniform and compact.

The XRD pattern exhibits only the (112), (200), and (220) diffraction lines of kesterite CZTS (JCPDS26-0575). The (312) diffraction line of kesterite CZTS was also detected at 2θ = 55.7°, not shown in Fig. 2(a). Two minor lines appearing at 2θ = 25.4° and 2θ = 42.5° are attributed to MoO_3 and MoS_2, respectively.

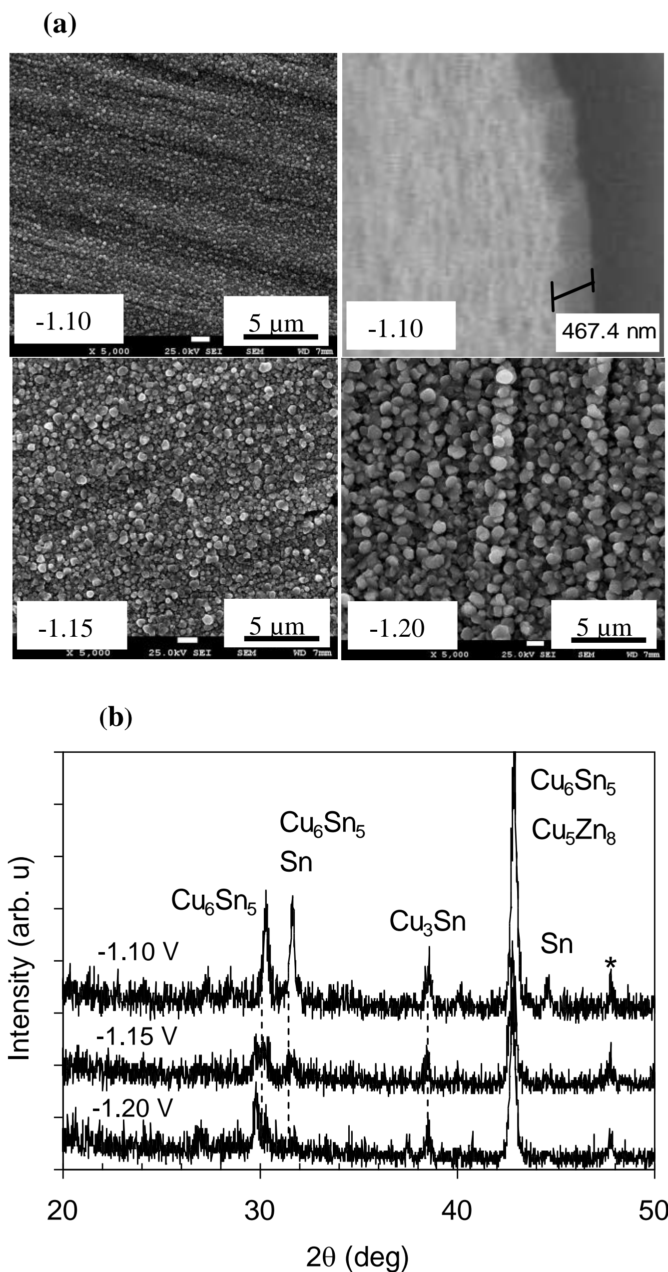

Figure 1. (a) SEM plan view and (b) XRD plots of the argon-annealed Cu-Zn-Sn (CZT) metallic alloy films electrodeposited at different cathode potentials.

From the width of the (112) diffraction line and using the scherrer equation the size of crystallites, from which the grains are formed, was estimated as 27 nm. The presence of ZnS and Cu_2SnS_3 (CTS) secondary phases in CZTS cannot be discarded based on the XRD results. The XRD lines of these two phases almost overlap with the CZTS lines. The detection of ZnS and CTS impurity

phases in CZTS is normally performed by Raman spectroscopy. The Raman plot of the same sample as for Fig. 2(a) is illustrated in Fig 2(b). Apart from the CZTS-related peaks and shoulder, no other lines are shown to indicate the presence of impurity phases, at least within a depth of ~ 150 nm blow the film surface. The effective penetration depth of the Raman excitation wavelength used (512 nm) is 150 nm in CZTS [16]. The Raman peaks and shoulders appearing at 233.9 cm^{-1}, 284.2 cm^{-1}, 332.7 cm^{-1}, and 355.4 cm^{-1} can be assigned to the vibrational modes of kesterite (KS) and stannite (ST) structures of CZTS reported in [17] as 235.4 cm^{-1} (ST, E-mode), 284.3 cm^{-1} (KT, A-mode), 334.1 cm^{-1} (ST, A_1-mode), and 355.8 cm^{-1} (KT, B-mode), respectively. The relatively broad Raman peaks shown in Fig. 2(b) indicate the lack of high structural quality of the sample [18]. CTS has two major peaks at 303 cm^{-1} and 356 cm^{-1} showing almost the same intensities [16]. If the shoulder that appears at 355.4 cm^{-1} in Fig. 2(b) represents CTS, we would also expect to detect a peak at 303 cm^{-1}, which is not the case. Therefore, the CZTS films are free from CTS impurity phase. ZnS has a minor Raman peak at 275 cm^{-1} and a major peak at 352 cm^{-1} [16]. The latter peak is in the vicinity of the shoulder appearing at 355.4 cm^{-1} in Fig. 2(b) which was assigned to the vibrational B-mode of kesterite CZTS. Therefore, the presence of ZnS impurity phase in CZTS films can not be ruled out with absolute certainty. Fig. 2(c) and its inset show the current-voltage (IV) characteristic and the configuration of diodes prepared on CZTS.

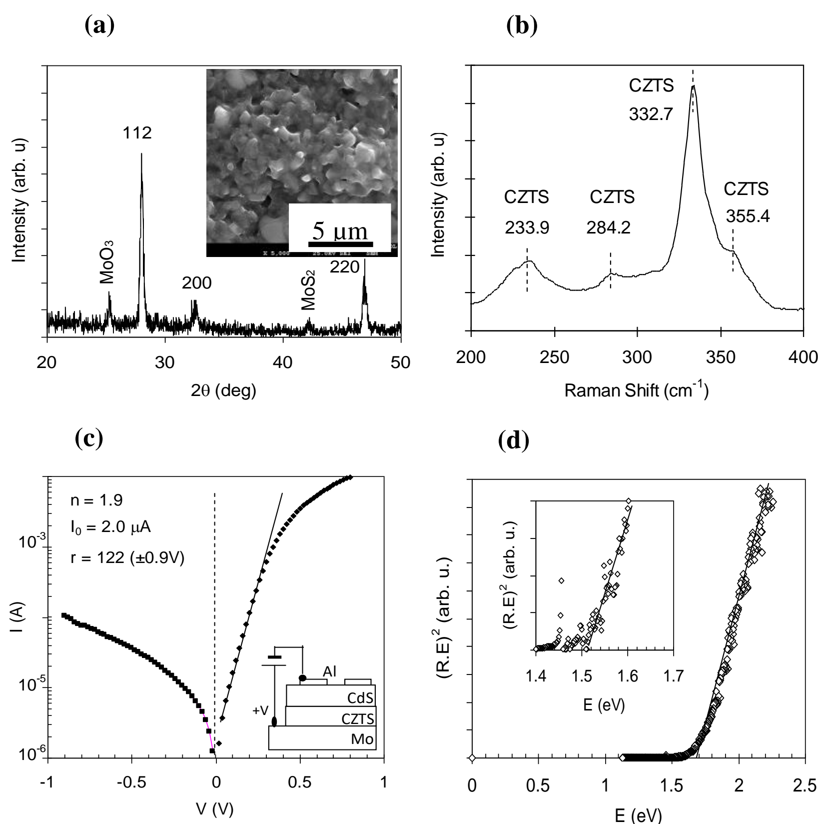

Figure 2. (a) The XRD spectrum and SEM plan view (inset) of a CZTS film. (b) The Raman spectrum of the same CZTS film. (c) The current-voltage plot of a CdS/CZTS diode with the configuration shown in the inset. (d) The variation of R, diode short-circuit photocurrent normalized to the incident photon flux, with the incident photon energy E.

The positive polarity of Mo substrate that corresponds to the forward current indicates the formation of a p-n junction at the interface of p-type CZTS and n-type CdS. The Mo substrate and Al top contact provide ohmic contacts to CZTS and to CdS, respectively. The current rectification factor (ratio of forward to reverse current) is r = 122 at ±0.9 V. From the fit of the forward IV relationship to the theoretical model some of the junction parameters were evaluated. The IV equation for a heterojunction is similar to that for a Schottky barrier diode and is generally dominated by thermionic emission of one type of carrier over an effective barrier height Φ. The IV relationship is given as $I = I_o[\exp(qV_j/nkT) - 1]$, where $I_o = AA^*T^2\exp(-\Phi/kT)$ [19]. Here, q is the electronic charge, n is the ideality factor, k is Boltzmann's constant, T is the absolute temperature, V_j is the voltage drop across the junction ($V_j = V - IR_s$), and R_s is the diode series resistance. A is the device area, and A^* (= 63.6 $Acm^{-2}K^{-2}$) is the effective Richardson constant for CZTS. From the fit of the forward IV plot in Fig. 2(c) to the IV equation, the diode parameters were determined as n = 1.9, I_o = 2.0 μA, and Φ = 0.41 eV. The reverse biased IV characteristic is of the space charge limited type where I varies in proportion to $V^{1.4}$. The diode short-circuit photocurrent normalized to the incident photon flux, R, that varies in proportion to the film optical absorption coefficient was measured at different incident photon energies E. A plot of $(R.E)^m$ against E is expected to yield a straight line whose intercept with the E axis measures a direct transition energy for m = 2 and indirect transition energy for m = 1/2. Fig. 2(c) and its inset illustrate such plots which yield two direct transition energies of 1.5 eV and 1.7 eV. The former value is generally taken as the band gap of CZTS. This is either a transition from the Cu_{Zn} defect level (E_V + 0.12 eV) to the conduction band (E_V + 1.64 eV) of kesterite CZTS, or a transition from the split valence band (E_V - 0.15 eV) of stannite CZTS to its conduction band (E_V + 1.33 eV) [15]. The measured transition energy of 1.7 eV is likely a transition from the valence band to the conduction band (E_V + 1.64 eV) of kesterite CZTS [15].

3.3. CZTSe films

The selenized precursor films had also a compact and uniform structure. The SEM plan view and cross section view of a CZTSe film are shown in the inset of Fig. 3(a). Selenization lead to the coalescence of the grains of precursor film. The XRD diffraction lines shown in Fig. 3(a) are attributed to the (112) and (204) lines of CZTSe (ICDD 04-010-6295) and to Mo (ICDD 00-042-1120), and $MoSe_2$ (ICDD 04-006-2098) [20]. The line visible at 2θ = 24.6° is attributed to MoO_3. The (312) line of CZTSe that is not shown in Fig. 3(a) was detected at 2θ = 54.0°. From the width of the (112) line and using the Scherrer equation the size of the crystallites was estimated as 28 nm. Fig. 3(b) shows the Raman spectrum of the same sample as for Fig. 3(a). The broad Raman band which extends from ~156 cm^{-1} to ~281 cm^{-1} and peaks at 203.7 cm^{-1} is the merge of individual CZTSe Raman lines which are reported to be in the close vicinity of 160 cm^{-1}, 168 cm^{-1}, 173 cm^{-1}, 194 cm^{-1}, 197 cm^{-1}, 232 cm^{-1}, and 236 cm^{-1} [8,20]. Among these lines, the most intensive one appears at 197 cm^{-1} which is assigned to the vibrational A mode of kestrite CZTSe (193 cm^{-1}) [17]. The peak position at 203.7 cm^{-1} in Fig. 3(b) shows a slight shift from 197 cm^{-1} apparently due to the structural disorder of the film. The shoulder shown at 231.1 cm^{-1} in Fig. 3(b) is attributed to the vibrational E-mode of kesterite CZTSe (233.0 cm^{-}

[1]) [17]. The widening of the individual Raman lines to form a single broad band indicates that the sample lacks high structural quality [8,21]. This can be due to the presence of the $CZTSe_xS_{1-x}$ secondary phase in the film as a result of contamination of the graphite box with sulfur during the sulfurization of previous films. The box was used for the synthesis of both CZTS and CSTSe films.

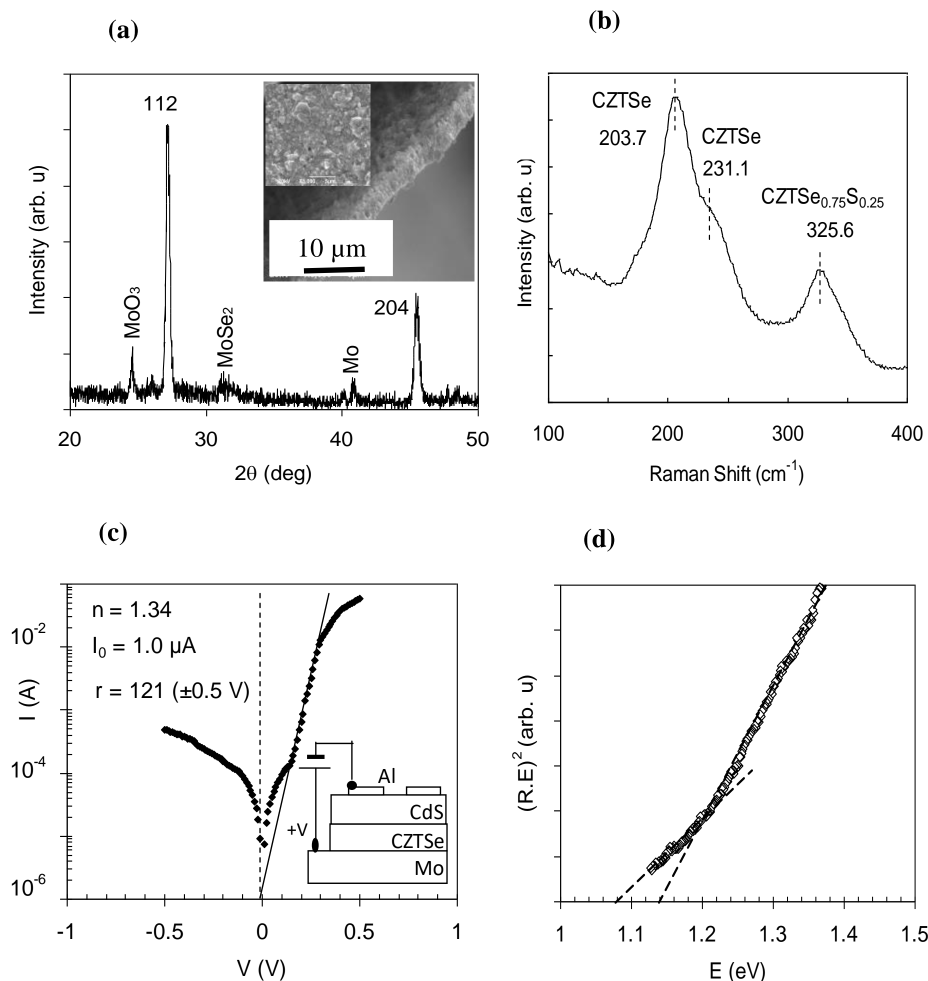

Figure 3. (a) The XRD pattern and SEM plan and cross section views (inset) of a CZTSe film. (b) The Raman spectrum of the same CZTSe film. (c) The current-voltage plot of a CdS/CZTSe diode with its configuration shown in the inset. (d) The variation of R, short-circuit photocurrent of diode normalized to the incident photon flux, with the incident photon energy E.

After each process the residual source material was removed and the graphite box was cleaned chemically. Decontamination of sulphur was more difficult and less efficient than that for selenium. The presence of $CZTSe_xS_{1-x}$ secondary phase in the film is evident from the Raman band centred at 325.6 cm^{-1}, Fig. 3(b), that corresponds to an alloy composition with $x = 0.75$ [18]. The Raman peaks of CZTSe films get broaden with the addition of sulfur to the film, which is related to the increase of structural disorder due to the random distribution of S and Se atoms in the lattice [18]. This explains well the reason for the broadening of the individual Raman lines which form the broad band centered at 203.7 cm^{-1} in Fig. 3(b). Similar to the case of CZTS films, p-CZTSe/n-CdS heterojunction diodes with a configuration shown in the inset of Fig. 3(c) were fabricated and their device parameters were

determined from their IV characteristics. The forward current in Fig. 3(c) corresponds to the positive polarity of Mo which verifies the formation of a p-n junction at the interface of CZTSe and CdS. The diode had a rectification factor of 121 (±0.5 V), ideality factor of n = 1.34, reversed bias saturation current of I_0 = 1.0 μA, and effective barrier height of Φ = 0.43 eV. A plot of the diode short circuit photocurrent normalized to the incident photon flux, R, against the incident photon energy, E, is depicted in Fig. 3(d). From the horizontal intercepts of the two straight line fits two direct transition energies of 1.08 eV and 1.14 eV were deduced. The former is assigned to the band gap of CZTSe, in agreement with the literature reports. The latter value is in excellent agreement with the band gap of the $CZTSe_xS_{1-x}$ impurity phase that is reported as 1.15 eV for x ~ 0.6 [22].

4. CONCLUSIONS

Non-porous and uniform CZT precursor films can be electrodeposited on Mo at a cathode potential of -1.20 V from a single solution that contains low concentrations of Cu (6 mM) and Sn (3 mM), and high concentration of Zn (200 mM). The precursor films can be converted to CZTS or CZTSe light absorber films by heat treatment in closed graphite box containing solid sulfur or selenium. The results of Raman spectroscopy, photocurrent spectroscopy and XRD analysis verify the obtainment of CZTS and CZTSe films. Heterojunction diodes with the reasonably good device parameters which were prepared from the absorber films signify the device quality of the synthesized films.

ACKNOWLEGMENTS
The authors would like to thank the Research Sector of Kuwait University for funding the research project RS01/13. We also acknowledge the valuable technical support received from the Science Nanoscopy Centre and the Research Sector Projects Unit (Project GS03/01).

References

1. X. Liu, Y. Feng, H. Cui, F. Liu, X. Hao, G. Conibeer, D. B. Mitzi and M. Green, *Prog. Photovoltaics* 24 (2016) 879–898.
2. S. K. Wallace, D. B. Mitzi and A. Walsh, *ACS Energy Lett.*2 (2017) 776–779.
3. K. Yu and E. A. Carter, *Chem. Mater.* 28 (2016) 4415–4420.
4. W. Wang, M. T. Winkler, O. Gunawan, T. Gokmen, T. K. Todorov, Y. Zhu and D. B. Mitzi, *Adv. Energy Mater.* 4 (2013) 1301465.
5. L. Chen and C. Park, *Korean J. Chem. Eng.* 34 (2017) 1187–1191.
6. A. Tang, Z. Li, F. Wang, M. Dou, Y. Pan and J. Guan, *Appl. Surf. Sci.* 402 (2017) 70–77.
7. L. Dong, S. Cheng, Y. Lai, H. Zhang and H. Jia, *Thin Solid Films* 626 (2017)168–172.
8. R. Kondrotas, R. Juskenas, A. Naujokaitis, A. Selskis, R. Giraitis, Z. Mockus, S. Kanapeckaite, G.Niaura, H. Xie, Y.Sánchez and E. Saucedo, *Sol. Energy Mater. Sol. Cells* 132 (2015) 21-28.
9. M. Valdés, Y. Di Iorio, K. Castañeda, R. E. Marotti and M. Vázquez, *J. Appl. Electrochem.* 47 (2017) 755–765.

10. M. I. Khalil, R. Bernasconi, L. Pedrazzetti, A. Lucotti, A. Le Donne, S. Binetti and L. Magagnin, *J. Electrochem. Soc.* 164 (2017) D302-D306.
11. M. Benaicha, M. Hamla and S. Derbal, *Int. J. Electrochem. Sci.* 11 (2016) 4909-4921.
12. T. Hreid, J. Li, Y. Zhang, H. J. Spratt, H. Wang and G. Will, *RSC Adv.* 5 (2015) 65114-65122.
13. B. Unveroglu and G. Zangari, *Electrochemica Acta* 219 (2016) 664-672.
14. M. Guo , X. Zhu and H. Li, *J. Alloys Compd.* 657 (2016) 336-340.
15. A. E. Rakhshani, *J. Alloys Compd.* 675 (2016) 387-392.
16. P. A. Fernandez, P. M. P. Salome and A. F. deCunha, *J. Alloys Compd.* 509 (2011) 7600-7606.
17. A. Khare, B. Himmetoglu, M. Johnson, D. J. Norris, M. Cococcioni and E. S. Aydil, *J. Appl. Phys.* 111 (2012) 083707.
18. M. Grossberg, J. Krustok, J. Raudoja, K. Timmo, M. Altosaar and T. Raadik, *Thin Solid Films* 519 (2011) 7403-7406.
19. D. A. Neamen, *Semiconductor Physics and Devices: Basic Principles*, McGraw Hill (2003) New York, USA.
20. R. Kondrotas, R. Juškėnas, A. Naujokaitis, G. Niaura, Z. Mockus, S. Kanapeckaitė, B. Čechavičius, K. Juškevičius, E. Saucedod and Y. Sánchez, *Thin Solid Films* 589 (2015) 165-172.
21. F. Luckert, D. I. Hamilton, M. V. Yakushev, N. S. Beattie, G. Zoppi, M. Moynihan, I. Forbes, A. V. Karotki, A. V. Mudryi, M. Grossberg, J. Krustok and R. W. Martin, *Appl. Phys. Lett.* 99 (2011) 062104.
22. S. Bag, O. Gunawan, T. Gokmen, Y. Zhu, T. K. Todorov and D. B. Mitzi, *Energy Environ. Sci.* 5 (2012) 7060-7065.

© 2017 The Authors. Published by ESG (www.electrochemsci.org). This article is an open access article distributed under the terms and conditions of the Creative Commons Attribution license (http://creativecommons.org/licenses/by/4.0/).